https://doi.org/10.5194/egusphere-2026-3884
Preprint. Discussion started: 3 August 2026

A globally scalable, light data framework for flood-hazard mapping using open geospatial services

Igor Sieczkowski Moreira[1], Jonathan Corker[2], Mehran Eskandari Torbaghan[2], Fernando Dornelles[3], and Lélio Antônio Teixeira Brito[1]

[1]Department of Civil Engineering, Universidade Federal do Rio Grande do Sul, Porto Alegre, Brazil
[2]Department of Civil Engineering, University of Birmingham, Birmingham, UK
[3]Department of Hydromechanics and Hydrology, Universidade Federal do Rio Grande do Sul, Porto Alegre, Brazil

Correspondence: Igor Sieczkowski Moreira (igor.moreira@ufrgs.br)

Abstract. Flood-risk screening is often limited by the lack of globally consistent hazard layers, because detailed hydraulic models require local calibration, boundary conditions, and substantial computation. This study presents a light data framework that uses application programming interfaces to assemble global elevation, hydrography, and road-network data for flood-hazard susceptibility mapping. Height Above Nearest Drainage is derived with drainage calibration constrained by OpenStreetMap hydrography, while the Multiresolution Index of Valley-Bottom Flatness adds complementary information on valley planarity. An interpretable monotonic gradient-boosted regression model is trained on return-period inundation inventories and converted into a common five-class ordinal hazard scale using threshold sets suited to planar and incised river settings. Applications to three independent river reaches show that the upper hazard classes consistently capture the 100-year flood footprint. The ordinal ranking remains physically coherent across return periods: low-susceptibility terrain is largely insensitive to increasing flood severity, whereas higher classes show progressively greater inundation likelihood. The model distinguishes flooded from non-flooded terrain in 78–83% of pairwise comparisons and remains effective under strict false-alarm constraints. The framework delivers screening-grade hazard layers for prioritisation and for integration with exposure and vulnerability analyses. Future work should test broader climatic and geomorphic settings and refine transferability across regions.

1 Introduction

Anthropogenic climate change has increased the frequency and severity of day-scale temperature extremes and has contributed to the widespread intensification of daily precipitation extremes (Zhang et al., 2013; Stocker, 2014). Globally, 1.8 billion people (roughly 23% of the world's population) live in areas directly exposed to a 1-in-100-year flood risk (McDermott, 2022). Given the severe and growing impacts of floods, traditional approaches to assessing flood risk are increasingly seen as insufficient; researchers are calling for more robust flood hazard and risk metrics to inform planning, public policy, and disaster risk management (de Bruijn et al., 2022; Azhar et al., 2025).

According to the Intergovernmental Panel on Climate Change (IPCC, 2023), flood risk is measured as the interaction of hazard, exposure, and vulnerability, where hazard refers to the potential occurrence of a natural or human-induced event that can cause harm to people, infrastructure, or the environment. Flood hazard is frequently assessed using high-resolution

https://doi.org/10.5194/egusphere-2026-3884
Preprint. Discussion started: 3 August 2026

hydrodynamic modelling, which—although accurate—demands extensive calibration data and computational resources that are rarely available or scalable (Andreadis et al., 2017; M. C. Rápalo et al., 2024). The unavailability of high-accuracy Digital Elevation Models (DEMs) and reliable precipitation data is one of the main limitations for assessing flood hazard in many developing countries (Kim et al., 2019).

More recently, machine learning (ML) approaches have been used as a practical, light data alternative to design-grade hydrodynamic modelling for inferring flood susceptibility from readily available geospatial predictors and event inventories. For example, the literature presents a range of ML approaches, including tree-ensemble learners (notably Random Forest and gradient-boosting variants), which capture non-linear terrain controls and exploit DEM-derived geomorphic indices alongside remote sensing systems (Navarro et al., 2025; Razavi-Termeh et al., 2025). In parallel, probabilistic classifiers provide lightweight and interpretable baselines by directly estimating inundation likelihood from conditioning factors, with Naïve Bayes remaining a common reference model (Tang et al., 2020).

Complementing the ML approach, geomorphological proxies derived from globally available DEM products can act as surrogates where detailed inputs are unavailable. In practice, moderate-resolution elevation data underpin rapid flood-extent mapping and can be coupled with post-event satellite imagery to delineate inundation and support damage screening (Werner, 2001; Merwade et al., 2008; Gianinetto et al., 2006). More generally, proxy layers from remote sensing and DEM-derived metrics are often combined within multi-criteria geographic information system (GIS) workflows, where indicators are standardised and weighted to produce hazard indices (Islam and Sado, 2000; Brivio et al., 2002; Wang et al., 2002, 2011).

Nevertheless, an end-to-end, globally standardised hazard-mapping pipeline that avoids region-specific tuning remains uncommon. ML studies are typically calibrated against local flood inventories and are explicitly linked to local geo-environmental characteristics (Navarro et al., 2025; Razavi-Termeh et al., 2025; Tang et al., 2020). Even DEM-driven flood-extent mapping is sensitive to grid resolution and the representation of hydraulic controls, so globally available elevation data can introduce artefacts (Werner, 2001; Merwade et al., 2008).

Motivated by these gaps, the aim of this paper is to present and evaluate a light data framework that assembles globally available datasets, retrieved via application programming interfaces (APIs) into an automated, open-source flood-hazard workflow. The approach uses open and interpretable geomorphology-informed predictors with a transparent tree-based learner that links terrain controls to observed inundation, avoiding site-specific hydrodynamic calibration while supporting conservative interpolation and extrapolation. The framework returns standardised hazard indices and maps designed for direct coupling with exposure and vulnerability within IPCC-consistent risk workflows. Section 2 details the Materials and Methods, including the framework overview, data inputs and assumptions, the derivation of Height Above Nearest Drainage (HAND), Multiresolution Index of Valley-Bottom Flatness (MRVBF), and related predictors, the machine learning formulation with prototype-aware discretisation, and the validation and sensitivity protocol. Section 3 presents and discusses the results for calibration and independent validation reaches, including performance diagnostics and behavioural assessment. Section 4 concludes with practical implications and priorities for further development.

https://doi.org/10.5194/egusphere-2026-3884
Preprint. Discussion started: 3 August 2026

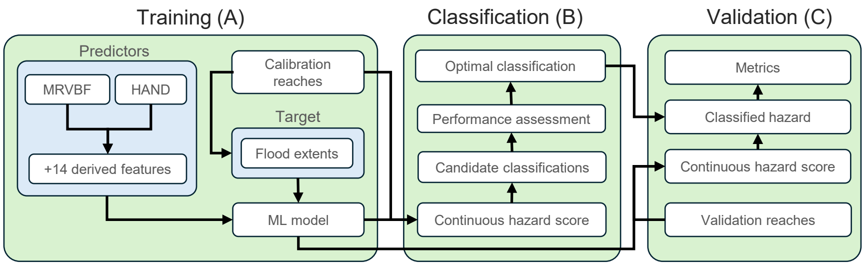

Figure 1. Methodology overview flowchart

2 Materials and methods

The methodology proposed in this study is organised into three stages: A) training, B) classification, and C) validation (Fig. 1). In stage A), a supervised machine-learning model is trained to predict a continuous hazard score using predictor variables selected from the literature and inventories of flood extents as target data (see Subsect. 2.2). Thus, the former provide the explanatory inputs for model fitting, whereas the latter are used exclusively as supervision data. Stage B) evaluates the most suitable number of classes for reclassifying the continuous output into a product that is both easily interpretable and physically meaningful. Finally, stage C) validates both the trained model and the selected classification scheme through a case study in areas hereafter referred to as validation reaches, which are distinct from those used for calibration and likewise include an independent inventory of flood extents.

2.1 Hazard framework overview

Following the risk conceptualisation adopted by the Intergovernmental Panel on Climate Change IPCC (2023), the framework developed in this study focuses exclusively on the hazard component, consistent with the aim of inferring flood susceptibility from geomorphological landscape controls rather than modelling the broader socioeconomic and infrastructural conditions that shape risk. To consider data-scarce scenarios, a qualitative approach is adopted. Previous studies have demonstrated the effectiveness of such qualitative approaches, showing that susceptibility zones can be delineated reliably from terrain variables alone (Miranda et al., 2023; Saravanan and Abijith, 2022).

Within this framework, globally available raw datasets, including Copernicus DEM GLO-30 elevation data and OpenStreetMap (OSM) hydrographic features, are programmatically retrieved and preprocessed to generate the main geomorphological predictors, HAND and MRVBF, as well as the remaining derived variables used by the machine learning model. These predictor layers constitute the explanatory inputs to the model, whereas flood-extent inventories are used only during calibration and validation as supervision and reference data, respectively. Model inference produces a continuous susceptibility surface representing the hazard component. For ease of interpretation, this surface is subsequently reclassified into five ordinal classes, following an approach similar to that adopted by Saravanan and Abijith (2022). Hereafter, the term susceptibility refers

https://doi.org/10.5194/egusphere-2026-3884
Preprint. Discussion started: 3 August 2026

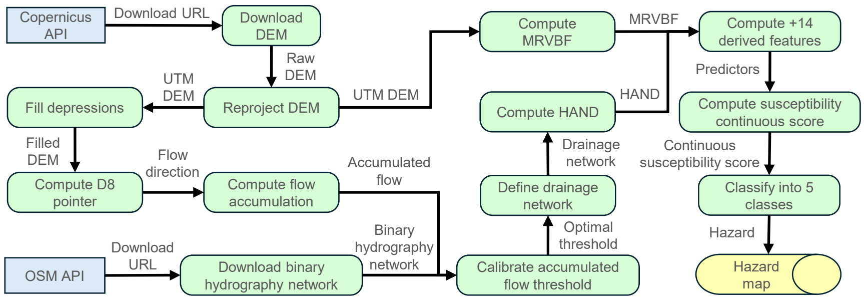

Figure 2. Hazard data flow diagram

to the continuous score and the underlying geomorphological propensity it represents, whereas hazard designates the classified five-class product and the overall framework output. Figure 2 summarises the hazard framework as a data flow diagram.

2.2 Hazard framework assumptions and inputs

The hazard framework is based on several assumptions. First, a $\sim 30\,\mathrm{m}$ global DEM is assumed to be sufficient to capture mesoscale controls on inundation over areas ranging from tens to hundreds of square kilometres, while recognising that micro-topography and small hydraulic structures may remain unresolved (Fatdillah et al., 2022; Guillaume Courty et al., 2019; van Ginkel et al., 2021). Second, predictors are restricted to geomorphological variables, consistent with their widespread use in the literature (Huang et al., 2017; Johnson et al., 2019; Esfandiari et al., 2020); accordingly, the outputs represent a screening-level propensity surface rather than an event-specific hazard realisation, and therefore do not replace calibrated hydrodynamic simulations where design-grade precision is required. Finally, we assume that OSM features are sufficiently complete and accurate at the study scale, with residual positional errors being small relative to the spatial resolution and intended application.

Also, the framework adopts a common map projection for all GIS files. Datasets are reprojected to a single coordinate reference system (CRS), defined by the centroid of the DEM. The CRS is specified by the Universal Transverse Mercator (UTM) zone, the WGS84 datum, and the hemisphere in which the centroid is located. The UTM zone is computed from centroid longitude using the standard rule. The hemisphere flag is set to north if latitude $\geq 0°$ and south otherwise.

The input datasets serve two distinct purposes within the hazard framework: i) to derive geomorphological predictors of inundation propensity, and ii) to provide supervision and reference data for model training and validation. The former are required both for model development and for subsequent application of the framework, whereas the latter are used exclusively during the learning and evaluation stages. All datasets to apply the framework are retrieved via API, whereas the learning and evaluation datasets are provided by the State Foundation for Metropolitan and Regional Planning (Metroplan). To ensure internal consistency and reproducibility, all layers are harmonised to a common spatial resolution, single CRS and expressed in SI units.

https://doi.org/10.5194/egusphere-2026-3884
Preprint. Discussion started: 3 August 2026

Three input datasets are used: i) the Copernicus GLO-30 DEM at 30 m resolution, as the primary geomorphological source; ii) open hydrographic features (rivers, streams, lakes, canals) from OSM, supporting drainage enforcement and proximity metrics; and iii) return-period (RP) flood-extent maps produced by Metroplan, used exclusively as supervision and reference data for calibration and validation.

The two DEM-derived predictors are introduced in Sect. 2.2.1, and the complete set of derived predictors is detailed in Sect. 2.2.2.

2.2.1 Geomorphological predictors

The proposed model represents hazard as a function of two complementary geomorphological DEM-derived descriptors: i) HAND, capturing relative vertical position with respect to the channel network; and ii) the MRVBF, capturing planar, depositional environments across nested spatial scales. Both indices are computed from the pre-processed topography and hydrography described in Sect. 2.2, using an automated workflow built on open-source geospatial libraries and command-line tools. Below we detail the conceptual background and operational implementation of each index.

HAND. Originally proposed by Rennó et al. (2008) and further formalised by Nobre et al. (2011), HAND expresses, for each DEM cell, the vertical distance to the nearest drainage pixel measured along the downslope flow path rather than in Euclidean space. Because HAND normalises topography relative to the drainage network and has shown hydrological relevance across catchments and spatial scales, it has been used as a parsimonious proxy for flood susceptibility, often in combination with complementary datasets or modelling components in order to address the limitations of topography-based screening (Nobre et al., 2011; Aristizabal et al., 2023). For this reason, HAND was selected in this study as one of the main variables for delineating potential inundation zones in data-scarce regions, given its global availability and rapid acquisition via API.

A first methodological innovation of this work concerns the HAND drainage network: instead of adopting a single ad hoc flow-accumulation threshold, we selected the threshold by iteratively maximising agreement with an external, independent binary river mask derived from OSM. This OSM-constrained optimisation reduces the known sensitivity of HAND to channel misplacement, especially in low-relief settings where small routing errors propagate into systematic bias (Zhang and Huang, 2009; Sabeh et al., 2025).

First, the DEM is hydrologically conditioned through standard preprocessing (sink filling, flow-direction and flow accumulation), yielding a flow-accumulation raster (F) for all cells in the domain. In parallel, the open hydrographic features (rivers and streams) are rasterised from OSM and converted into a binary mask of river pixels. A Euclidean distance transform is then applied to this mask to obtain, for each cell, the distance to the nearest mapped river pixel. A maximum search distance of $1\,\mathrm{km}$ is imposed so that the calibration focuses on kilometre-scale alignment between DEM-derived and mapped channels.

Let $F_{\max}$ denote the maximum value of flow accumulation in the domain. Candidate flow-accumulation thresholds are defined as fixed percentages of $F_{\max}$ between 0.01 % and 50 %. For each candidate (τ), all cells with $F \geq \tau$ are flagged as channels, and two quantities are counted: i) the total number of DEM-derived channel cells, $N_{\mathrm{chan}}(\tau)$; and ii) the number of these cells that fall within $1\,\mathrm{km}$ of an OSM river, $N_{\mathrm{match}}(\tau)$. The spatial agreement between DEM-derived channels and

https://doi.org/10.5194/egusphere-2026-3884
Preprint. Discussion started: 3 August 2026

mapped hydrography is then expressed as a similarity score (Eq. (1)).

$$S(\tau) = 100 \cdot \frac{N_{\mathrm{match}}(\tau)}{N_{\mathrm{chan}}(\tau)} \tag{1}$$

Which represents the percentage of extracted channel pixels that match with the OSM river network. Finally, the optimal flow-accumulation threshold is chosen as the value that maximises $S(\tau)$ over the set of candidates. The corresponding thresholded flow-accumulation raster defines the final drainage network used as input for HAND computation through the open-source WhiteboxTools library.

MRVBF. The MRVBF, introduced by Gallant and Dowling (2003), identifies valley bottoms and depositional environments where runoff decelerates and floodplain formation is favoured by combining planarity and relative topographic position across multiple DEM scales (Guerschman et al., 2011; Huang et al., 2017). Given its rapid acquisition via API, MRVBF was selected alongside HAND as a primary variable for delineating potential inundation zones in data-scarce regions.

At each analysis scale, the algorithm classifies DEM cells according to local slope and curvature criteria into "flat" and "non-flat". The final MRVBF value for a cell is the number of scales at which it is classified as "flat". In this study, MRVBF therefore assumes values in the range 0–7 (six resolutions + the finest-scale level), with higher scores indicating persistent flatness across scales and hence a stronger potential flood-storage areas.

A key parameter is the slope threshold (T_{SLOPE}), defined as a function of the effective DEM resolution (Eq. (2); Gallant and Dowling, 2003), where r_{m} is the arithmetic mean of the grid spacing. To ensure a consistent six-level configuration, the maximum analysis scale was derived from tile size and window radius, and DEM tiles were retrieved at the largest size permitted by the API before clipping to the target domain.

$$T_{\mathrm{SLOPE}} = 116.57 \cdot r_{\mathrm{m}}^{-0.62} \tag{2}$$

2.2.2 Derived predictors

In addition to the primary indices, the hazard model ingests a compact set of secondary predictors derived from these fields together with the DEM and the hydrographic mask. The aim is to enrich the feature space while retaining physical interpretability. Predictors are organised into four families: i) channel proximity, ii) local and reach-scale valley-floor planarity, iii) HAND–planarity combinations, and iv) normalised HAND metrics, which are described in the following subsections.

Channel-proximity metrics. Channel cells are identified via a binary indicator, C_{ch}, derived from the hydrographic layer. The Euclidean distance to the nearest channel cell, D_{ch}, is log-transformed (Eq. (3)) to reflect the non-linear decay of channel influence with lateral separation (Graf, 1984). A complementary buffer indicator, B_{ch}, flags pixels within $D_{\mathrm{ch}} \leq 100\,\mathrm{m}$, delineating the riparian corridor most strongly governed by channel–floodplain connectivity (Zhao et al., 2017; Bohorquez and Del Moral-Erencia, 2017).

$$\log D_{\mathrm{ch}} = \log(1 + D_{\mathrm{ch}}) \tag{3}$$

Local and reach-scale planarity of valley floors. Strongly planar pixels are characterised as $\mathrm{MRVBF} \geq 6$ (since 7 indicates planarity across all resolutions, while 6 fails the planarity criterion at only one scale). A moving-window aggregation ($\sim 100\,\mathrm{m}$,

https://doi.org/10.5194/egusphere-2026-3884
Preprint. Discussion started: 3 August 2026

consistent with regional inundation modelling resolutions (Peña et al., 2021)) converts this mask into the local floodplain fraction, $F_{\mathrm{pl}} \in [0,1]$, i.e. the proportion of strongly planar pixels in the neighbourhood. This captures sub-kilometre variability in valley-bottom morphology relevant to floodplain connectivity and attenuation (Vázquez-Tarrío et al., 2024).

To incorporate river-specific context, two reach-scale descriptors summarise MRVBF within the buffered corridor ($B_{\mathrm{ch}} = 1$): P_{ctx}, the mean fraction of strongly planar pixels in the buffer, and $M_{\mathrm{ctx},90}$, the 90th percentile of MRVBF therein. Although constant within a calibration reach, these variables encode systematic contrasts between confined valleys and wide alluvial floodplains, consistent with hydro-geomorphic controls on flood propagation and sediment routing (Guan et al., 2016; Cunha et al., 2017; Peña et al., 2021).

HAND–planarity combinations. Because a given height above channel can imply different hazard levels across contrasting valley forms (Peña et al., 2021; Cunha et al., 2017), HAND is complemented by planarity-modulated variants based on F_{pl} (Eq. (4)–(6)).

$$H_{\mathrm{adj},1} = \frac{\mathrm{HAND}}{1 + 0.75 \cdot F_{\mathrm{pl}}} \tag{4}$$

$$H_{\mathrm{adj},2} = \mathrm{HAND} \cdot (1 - 0.5 \cdot F_{\mathrm{pl}}) \tag{5}$$

$$H_{\mathrm{eff}} = \frac{\mathrm{HAND}}{10^{-3} + F_{\mathrm{pl}}} \tag{6}$$

Eq. (4)–(6) reduce the effective vertical separation in predominantly planar settings while preserving higher values in dissected terrain; H_{eff} further accentuates contrasts where F_{pl} approaches zero (Cunha et al., 2017). An additional interaction term, HAND × MRVBF, captures the joint influence of vertical position and valley-floor morphology, discriminating settings that share similar HAND values but differ in storage capacity (Peña et al., 2021; Vázquez-Tarrío et al., 2024).

Normalised HAND metrics. To enhance transferability, HAND is also expressed in dimensionless forms as a standardised z-score, H_z (Li et al., 2023), and a percentile rank, $H_{\mathrm{rank}} \in [0,1]$, defined as the empirical cumulative distribution function of reach-wise HAND. Both remove dependence on absolute elevation units, a common practice in tree-ensemble flood-mapping frameworks (Hajji et al., 2025).

2.3 Model training

A histogram-based gradient-boosting regressor (HGBR) was selected for model training with monotonic constraints. We cast hazard prediction as an ordinal regression problem: return-period classes from the target maps are harmonised into a universal ladder and re-labelled as ordered integers. The HGBR is trained on these labels as a continuous response, producing a scalar susceptibility score, $\hat{s}$, that is monotonically related to the underlying ladder; discrete classes are recovered by thresholding $\hat{s}$.

HGBR was adopted because the predictor set has the structure of a pixel-wise tabular matrix dominated by terrain variables, for which gradient-boosting methods have demonstrated strong performance in flood-hazard mapping (Saravanan and Abijith, 2022; Hajji et al., 2025; Razavi-Termeh et al., 2025), while also allowing monotonic constraints that enforce physically consistent response directions.

https://doi.org/10.5194/egusphere-2026-3884
Preprint. Discussion started: 3 August 2026

Training is conducted jointly on two calibration reaches (one predominantly planar and one entrenched) using the merged predictor matrix (including all predictors in Sect. 2.2.2). To address class imbalance, pixels receive spatial weights of 9 (in-channel), 4 (buffer), or 1 (elsewhere), with additional inverse-frequency class weighting. Background pixels within the lowest-RP flood extent and outside the buffer are down-sampled by 50 % to reduce computation, while all other pixels are retained.

The HGBR is fitted with squared-error loss and early stopping (internal validation fraction 0.1, patience 50). Hyperparameters are maximum 2000 boosting iterations, learning rate 0.07, maximum 63 leaf nodes per tree, minimum 200 samples per leaf, and ℓ_2 regularisation 10^{-3}; all runs use a fixed random seed (42).

The model was trained with monotonic constraints to enforce physically consistent relationships between selected predictors and the susceptibility score. The full predictor set and the corresponding monotonic constraints are summarised in Table A1. HAND, channel distance, and log-transformed channel distance were constrained to have non-increasing effects, reflecting the expected reduction in susceptibility with increasing vertical or lateral separation from the drainage network. In contrast, the in-channel indicator, the $100\,\mathrm{m}$ buffer indicator, and the local floodplain fraction were constrained to have non-decreasing effects. All remaining predictors were left unconstrained. These constraints reduced counter-physical responses, particularly in the presence of label noise.

2.4 Model classification

After training, the HGBR model was applied to the full predictor stack, without sub-sampling, to produce a continuous hazard score for both calibration rivers. This score was then discretised into K ordinal classes, where 1 denotes the lowest susceptibility and K the highest. Candidate classifications from $K = 3$ to $K = 6$ were tested. For each K, class thresholds were derived separately for the two calibration rivers. Within each prototype, thresholds were defined from equally spaced empirical quantiles of the continuous score, from the $1/K$ quantile to the final threshold at the $(K-1)/K$ quantile. In addition, each prototype was described by a score signature based on the 10th, 30th, 50th, 70th, and 90th empirical quantiles of the same score distribution. These two components serve complementary purposes: the thresholds define the class limits for a given K, whereas the signatures describe the distributional profile of each prototype and support transfer to new reaches. For a new reach, its score signature is compared with those of the two prototypes, and the operational thresholds are taken from the closest prototype or obtained by weighted interpolation between both threshold sets. Pixels mapped as active channel ($C_{\mathrm{ch}} = 1$) are assigned to the highest hazard class to preserve physical consistency.

For each candidate number of classes, the resulting ordinal hazard maps were validated against a binary flood indicator for each return period of the Metroplan reference flood extents described in Sect. 2.2. For every tested value of K, performance was assessed using the following metrics: i) monotonicity of flood occurrence across classes, evaluated by Cochran–Armitage trend test; ii) temporal ordering of inundation across return periods, through Kendall's rank correlation coefficient τ and survival-type curves; and iii) discrimination and probabilistic accuracy assessed by receiver-operating characteristic (ROC) curves and the associated area under the curve (AUC) and partial area under the curve (pAUC).

Finally, overall probabilistic accuracy is summarised by the Brier score and its classical decomposition into reliability, resolution and uncertainty components, computed over the full set of pixels, classes and RPs using the joint logistic predictions.

https://doi.org/10.5194/egusphere-2026-3884
Preprint. Discussion started: 3 August 2026

Table 1. HAND drainage calibration against OSM hydrography

Reach	τ^* (% of $F_{\max}$)	τ^* (abs., F)	$S(\tau^*)$ (%)
Gravataí	23.1	231,078	100
Sinos	6.9	68,434	94.4

2.5 Model validation

With the model trained and the number of classes defined, the final methodological step was external validation through an independent case study. To this end, three additional rivers (i. Paranhana, ii. Jacuí and iii. Areia), outside the calibration domain, were selected because Metroplan reference flood extents were also available for them. This allowed the model to be evaluated on reaches that were not involved in calibration, thereby enabling the identification of potential calibration bias and a more rigorous assessment of transferability. The same metrics adopted in the model classification stage (Sect. 2.4) were then applied.

3 Results and discussion

The results are presented following the same sequence adopted in the methodology and summarised in Fig. 1. Accordingly, each subsection corresponds to one stage of the proposed workflow, allowing the progression from model training, classification, and validation to be reported.

3.1 Model training

The combination of HAND and MRVBF is particularly complementary: HAND represents the local vertical terrain-drainage separation, whereas MRVBF captures the accommodation space and planform diffusion that elevation difference alone cannot resolve. Here, both are derived from a DEM retrieved via API, ensuring reproducibility and minimising human error.

For each calibration reach, the optimal flow-accumulation threshold, τ^*, is reported in Table 1 both as a fraction of the maximum flow-accumulation value within the domain, $F_{\max}$, and as the corresponding absolute flow-accumulation value. The table also presents the associated match percentage, $S(\tau^*)$, computed within a search distance of $1\,\mathrm{km}$.

For both calibration reaches, the drainage network achieved near-perfect spatial agreement with the mapped hydrography, with match percentages of 100 % and 94.4 % for the Gravataí and Sinos reaches, respectively; this strong correspondence between the DEM-derived flow network and the observed river locus strengthens the physical interpretation of HAND as a proxy for inundation propensity while reducing artefacts from spurious channels and disconnected segments.

DEM context together with the resulting MRVBF and HAND patterns for the two calibration reaches are summarised in Fig. 3.

https://doi.org/10.5194/egusphere-2026-3884
Preprint. Discussion started: 3 August 2026

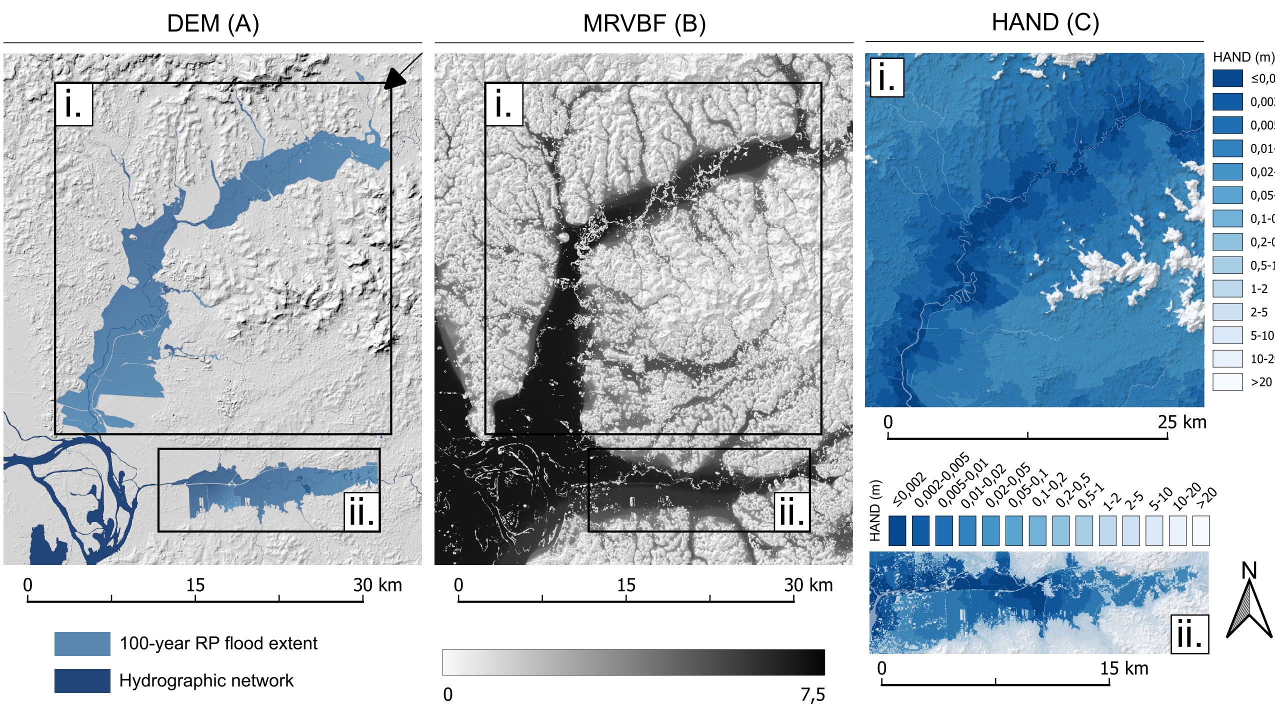

Figure 3. Calibration reaches and geomorphological indices. Copernicus DEM GLO-30 data courtesy of ESA Copernicus. © Metroplan. All rights reserved.

Accordingly, in panel A–B, despite the contrasting geomorphic settings of the calibration rivers, MRVBF remains jointly representable within a single panel without loss of interpretability. By contrast, in panel C, HAND spans distinct dynamic ranges across the rivers and therefore required separate visualisation to avoid scale dominance. Sinos exhibits an extensive low-HAND expanse (predominantly below 5 cm), consistent with a broad, weakly confined setting, whereas Gravataí transitions rapidly from low HAND in the immediate corridor to approximately 10–20 m over short lateral distances, indicating stronger confinement and steeper valley-side gradients. These divergent regimes motivated the explicit distinction between planar and incised prototypes, as any single global discretisation of the continuous susceptibility score would otherwise embed morphological bias. Nevertheless, part of the contrast may reflect domain size and DEM conditioning: the Sinos calibration window is substantially larger (approximately 6.4 times Gravataí), and sink-filling can behave differently across extents, potentially smoothing long-wavelength depressions and increasing apparent planarity.

The six-resolution MRVBF standardisation addresses a rarely discussed pitfall: without explicit scale control, changing spatial extent shifts the effective filter bank and yields extent-dependent magnitudes (Malone et al., 2018; Rahmani et al., 2022). A related effect is that DEM smoothing over extensive domains can attenuate local relief and reduce HAND-derived gradients (Dávila-Hernández et al., 2022; Erdbrügger et al., 2021), which helps explain the lower HAND values observed in

https://doi.org/10.5194/egusphere-2026-3884
Preprint. Discussion started: 3 August 2026

Table 2. Prototype signatures (quantiles of the continuous susceptibility score)

Prototype	q_{10}	q_{30}	q_{50}	q_{70}	q_{90}
(i) Planar	2.67	4.55	5.60	6.01	6.11
(ii) Incised	2.01	2.44	4.17	5.18	6.18

Sinos. The prototype-based classification accommodates this by contextualising HAND relative to the effective geomorphology of each domain rather than imposing a single global threshold.

3.2 Model classification

To implement the prototype-aware classification, each calibration reach was summarised by a compact score signature defined by the empirical quantiles q_{10}, q_{30}, q_{50}, q_{70}, and q_{90} of the continuous HGBR output, $\hat{s}$ (Table 2). For each prototype, class thresholds for a given K were derived from the empirical distribution of $\hat{s}$ at equally spaced quantiles, from $1/K$ to $(K-1)/K$. Because $\hat{s}$ aggregates the geomorphological controls into a single monotone susceptibility ordering, its quantile structure provides an informative descriptor of how susceptibility is distributed in space, capturing the degree of confinement. A further methodological innovation of this work is the use of two calibration reaches as anchoring extremes—Sinos and Gravataí—to operationalise this signature in a transferable classification scheme. For any target reach, the corresponding threshold vector can be selected by matching its signature to these anchors, or obtained by interpolation for intermediate morphologies. This yields prototype-consistent cut values to partition $\hat{s}$ into K ordinal classes.

The signatures clarify why a single global set of cuts would be systematically biased: the planar prototype concentrates scores towards high values ($q_{70} \approx q_{90}$), whereas the incised prototype exhibits a wider spread, so a global mapping would over-classify planar reaches and under-classify incised ones. Accordingly, the incised prototype requires lower $\hat{s}$ thresholds for every class transition, with the separation largest at low-to-intermediate susceptibility and converging near the channel.

With the resulting signatures, candidate discretisations with $K \in \{3,4,5,6\}$ classes were evaluated for both calibration reaches using the criteria presented in Sect. 2.4. In Sinos (Table 3), all candidates satisfy the trend criterion and maintain correct temporal ordering. Discrimination improves markedly up to $K = 5$, driven by increasing resolution rather than changes in calibration. Moving to $K = 6$ yields only negligible further gains but slightly weakens temporal ordering, increasing the violation rate.

In Gravataí (Table 4), the trend criterion is again satisfied. The $K = 4$ solution is consistently weakest, whereas $K = 3$ yields the strongest temporal ordering at the cost of a coarser scale. Although $K = 6$ attains the highest AUC, its gains over $K = 5$ are modest and accompanied by the highest violation rate.

Selecting K is therefore a trade-off between finer stratification and maintaining an interpretable ordinal scale that behaves monotonically with respect to observed flooding across return periods. We therefore retained $K = 5$ as a balanced choice: it

https://doi.org/10.5194/egusphere-2026-3884
Preprint. Discussion started: 3 August 2026

Table 3. Sensitivity to the number of classes K in Sinos

K	Trend	τ	Viol.	AUC	pAUC$_{0.20}$	Brier	Rel.	Res.
3	5/5	-0.489	0.0055	0.871	0.394	0.0802	0.0002	0.0388
4	5/5	-0.496	0.0076	0.911	0.581	0.0715	0.0002	0.0475
5	5/5	-0.498	0.0082	0.931	0.678	0.0657	0.0003	0.0534
6	5/5	-0.490	0.0093	0.931	0.679	0.0638	0.0004	0.0554

Table 4. Sensitivity to the number of classes K in Gravataí

K	Trend	τ	Viol.	AUC	pAUC$_{0.20}$	Brier	Rel.	Res.
3	4/4	-0.523	0.0436	0.801	0.421	0.1473	0.0013	0.0631
4	4/4	-0.486	0.0385	0.757	0.137	0.1571	0.0066	0.0587
5	4/4	-0.514	0.0435	0.813	0.229	0.1443	0.0050	0.0698
6	4/4	-0.509	0.0535	0.854	0.396	0.1437	0.0052	0.0706

preserves the correct ordering structure, avoids unnecessary fragmentation of the scale, and provides a clear five-level classification with stable behaviour across basins.

This choice is also consistent with common practice in flood-susceptibility mapping, where five ordered categories provide a well-established balance between detail and usability (Saravanan and Abijith, 2022; Costache et al., 2023; Badillo-Rivera et al., 2025).

Having adopted the five-class classification, we present the final performance metrics for the calibration rivers. The resulting equally spaced quantile class cut-offs are reported in Table 5.

Figure 4 provides a qualitative plausibility check by juxtaposing the final $K = 5$ hazard map, for i. Sinos and ii. Gravataí, with the Metroplan $\mathrm{RP} = 100$ flood extent, used as an external reference for hydrodynamically modelled flood connectivity.

Across both calibration reaches, the $\mathrm{RP} = 100$ footprint predominantly falls within Classes 4–5, consistent with a discretisation that compresses the continuous score $\hat{s}$ into an ordinal scale whose upper tail represents river-adjacent, hydraulically connected terrain. Residual disagreement is concentrated in anthropogenically modified corridors where hydraulic connectivity is altered by containment works (e.g. dikes and roads acting as barriers). These areas are highlighted in Fig. 4 together with the black-outlined exclusion zones removed from HGBR training, preventing the model from encoding engineered non-inundation as a geomorphic signal. Consequently, mild and interpretable degradation in AUC/pAUC may occur where validation labels incorporate barrier effects that the susceptibility layer is not designed to reproduce.

https://doi.org/10.5194/egusphere-2026-3884
Preprint. Discussion started: 3 August 2026

Table 5. Prototype-specific cut-off sets defining the five susceptibility classes

Prototype	Cut 1	Cut 2	Cut 3	Cut 4
(i) Planar	3.97	5.16	5.89	6.05
(ii) Incised	2.11	3.41	4.59	5.74

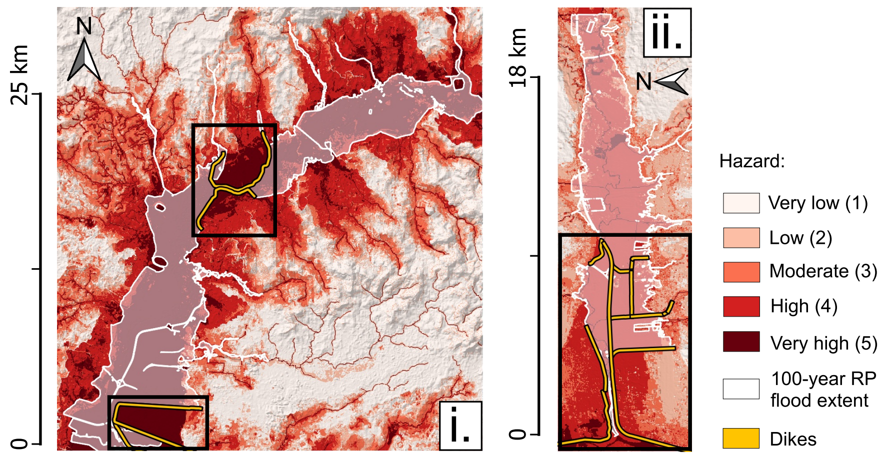

Figure 4. Hazard maps ($K = 5$) in the calibration reaches. Copernicus DEM GLO-30 data courtesy of ESA Copernicus. © Metroplan. All rights reserved.

The ROC families (Fig. 5) translate map-level coherence into discrimination performance across decision thresholds (Ahmad et al., 2025) and, by spanning multiple return periods, test whether the susceptibility ranking remains stable as hydrodynamic severity increases.

In Sinos, discrimination is consistently excellent across $\mathrm{RP} = 5$–$\mathrm{RP} = 100$ ($\mathrm{AUC} = 0.918$–0.932) with strong early-hit behaviour in the low false-positive rate (FPR) regime ($\mathrm{pAUC}_{\mathrm{FPR} \leq 0.20} = 0.125$–$0.138$; $\mathrm{pAUC}_{\mathrm{norm}} = 0.624$–$0.689$). In Gravataí, performance is slightly lower ($\mathrm{AUC} = 0.807$–0.824) and low-FPR gains are substantially smaller ($\mathrm{pAUC}_{\mathrm{FPR} \leq 0.20} = 0.043$–$0.051$; $\mathrm{pAUC}_{\mathrm{norm}} = 0.213$–$0.253$). For both rivers, the near constancy of AUC and pAUC across return periods indicates return-period invariance, supporting interpretation of the susceptibility pattern as a persistent expression of basin controls rather than an artefact of a specific event magnitude.

The pAUC at $\mathrm{FPR} \leq 0.20$ is decision-relevant because preparedness often operates under strict false-alarm budgets (Ahmad et al., 2025). In Sinos, the high pAUC confirms that alert zones can be delineated at low false-positive rates; in Gravataí, the lower values suggest that aggregation of the upper classes is preferable when false alarms are costly.

https://doi.org/10.5194/egusphere-2026-3884
Preprint. Discussion started: 3 August 2026

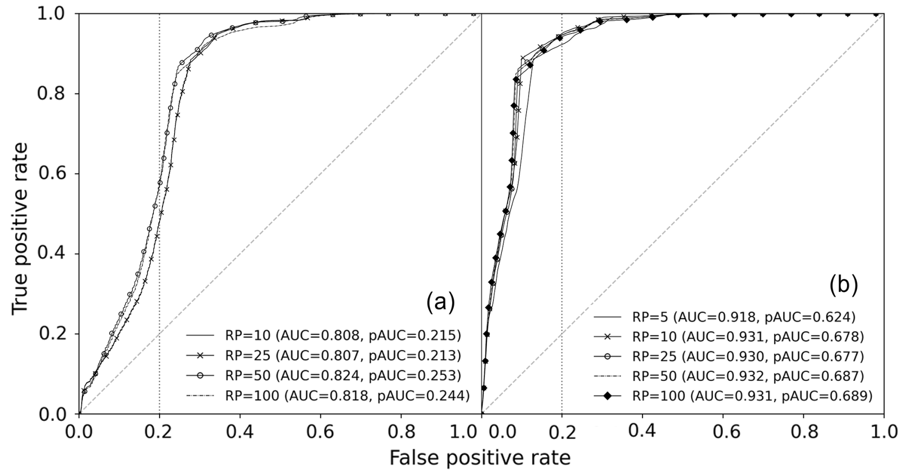

Figure 5. (a) Gravataí and (b) Sinos ROC curves

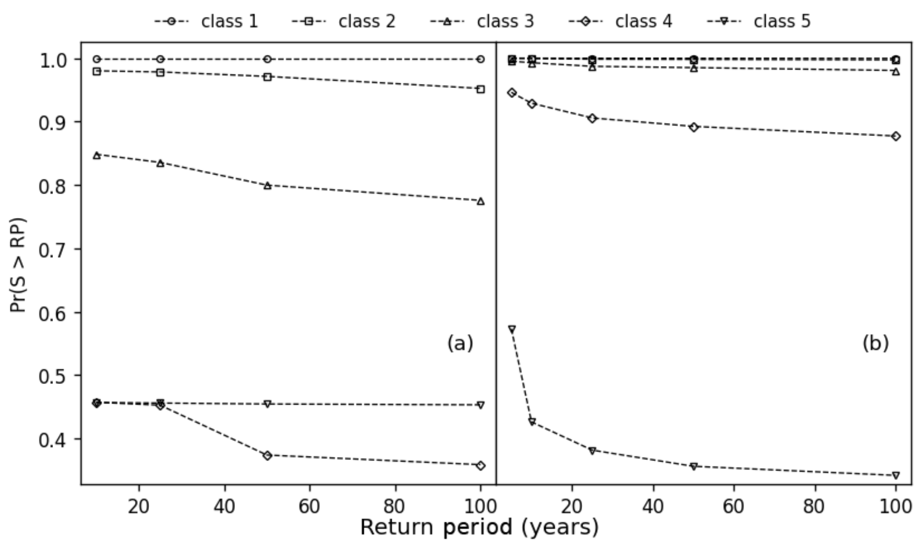

Figure 6. Survival-type curves $\Pr(S > \mathrm{RP})$ by class for the calibration reaches ($K = 5$)

Survival-type diagnostics $\Pr(S > \mathrm{RP})$ (Fig. 6) further test whether the ordinal classes preserve the temporal ordering of inundation as return period increases, consistent with multi-scenario flood-hazard practice in which maps across RP levels are compared to assess how extent and intensity evolve with event rarity (Albano et al., 2024; Tufano et al., 2023).

For Sinos, survival decreases monotonically with RP within each class and remains strictly ordered across classes: Class 1 is near invariant and close to unity, whereas Class 5 declines markedly (0.573 at $\mathrm{RP} = 5$ to 0.342 at $\mathrm{RP} = 100$), yielding wide and stable separation between low- and high-susceptibility terrain. For Gravataí, Classes 1–4 largely follow the expected orderings, but the upper tail reveals a limitation: Class 5 is weakly sensitive to RP and not cleanly separated from Class 4

https://doi.org/10.5194/egusphere-2026-3884
Preprint. Discussion started: 3 August 2026

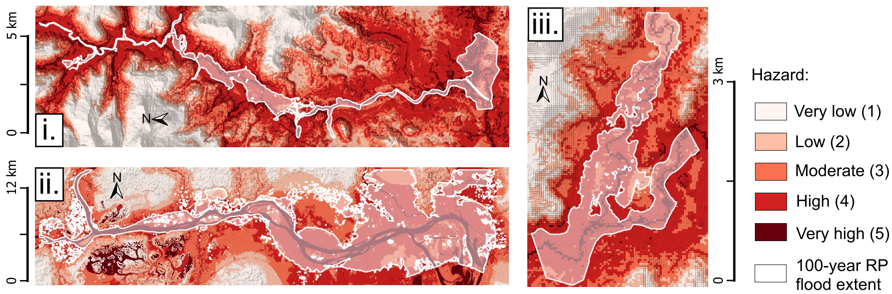

Figure 7. Hazard maps ($K = 5$) in the validation reaches. Copernicus DEM GLO-30 data courtesy of ESA Copernicus. © Metroplan. All rights reserved.

Table 6. External validation summary for $K = 5$ in the independent reaches

Reach	Trend	τ	Viol.	AUC	$\mathrm{pAUC}_{0.20}$	Brier	Rel.	Res.
(i) Paranhana	5/5	-0.274	0.0181	0.784	0.365	0.0558	0.0001	0.0076
(ii) Jacuí	5/5	-0.466	0.0590	0.827	0.389	0.1472	0.0032	0.0529
(iii) Areia	5/5	-0.448	0.0468	0.794	0.420	0.0840	0.0021	0.0357

(remaining ≈ 0.45 across $\mathrm{RP} = 10$–$\mathrm{RP} = 100$ and exceeding Class 4 at higher RP). Such heterogeneity is consistent with scenario studies, where some locations show negligible change at lower return periods but marked expansion at higher RP, while others exhibit modest incremental differences depending on controlling conditions (Tufano et al., 2023; Albano et al., 2024). Operationally, this indicates that in Gravataí the highest tier is best treated as a joint extreme zone and aggregated with Class 4 for preparedness mapping, whereas in Sinos the full five-class hierarchy remains behaviourally coherent and decision-useful.

3.3 Model validation

The trained susceptibility model and the prototype-aware $K = 5$ discretisation were transferred to three independent validation reaches. Figure 7 presents the resulting hazard map for i. Paranhana, ii. Jacuí, and iii. Areia, with the $\mathrm{RP} = 100$-year flood extent overlaid as a visual reference.

External performance was evaluated using the same validation suite adopted for the calibration reaches, with summary metrics reported in Table 6.

Across all independent reaches, the ordinal structure is preserved: the Cochran–Armitage trend test is satisfied for all return periods (5/5), Kendall's τ remains negative throughout, and violation rates remain stable. Temporal ordering is stronger in Jacuí and Areia ($\tau = -0.466$ and -0.448) than in Paranhana ($\tau = -0.274$), although it also shows the lowest violation rate (0.0181).

https://doi.org/10.5194/egusphere-2026-3884
Preprint. Discussion started: 3 August 2026

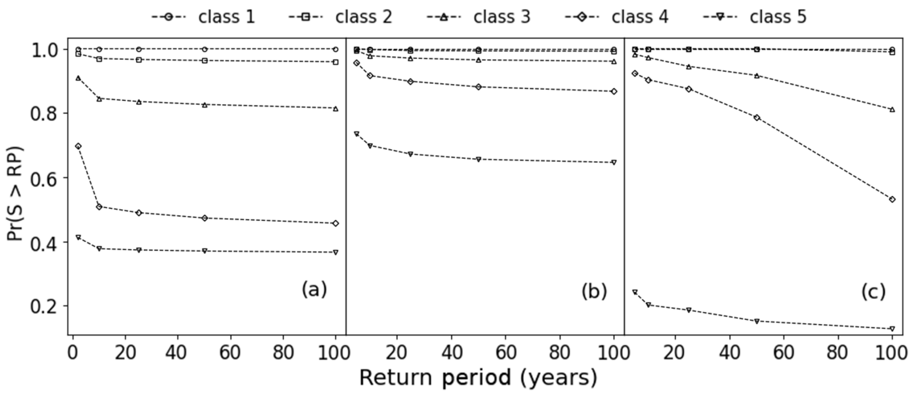

Figure 8. Survival-type curves $\Pr(S > \mathrm{RP})$ by class for the validation reaches ($K = 5$)

Discrimination also remains stable overall, with AUC values of 0.784–0.827, close to the Gravataí calibration benchmark ($AUC = 0.813$), indicating limited overfitting and preserved ranking skill outside the calibration domains. In the low-false-alarm regime, performance is strongest in Areia and Jacuí, where $\mathrm{pAUC}_{0.20}$ reaches 0.420 and 0.389, while Paranhana remains only slightly lower (0.365). The Brier decomposition shows that reliability errors are similar in all reaches, so differences in overall probabilistic performance are driven mainly by resolution: Jacuí achieves the strongest class separation (Res.=0.0529), whereas Paranhana combines the lowest Brier score and resolution, suggesting a more conservative but less contrasted class structure. Overall, the results support spatial transferability while showing that the strength of class-to-class separation varies across validation basins.

To complement this analysis, Fig. 8 presents the corresponding class-wise survival-type curves.

Across the three external validation reaches, the survival-type curves broadly reproduce the behavioural signatures observed for the calibration basins, thereby supporting once again the spatial transferability of the prototype-aware discretisation. In all cases, low-susceptibility terrain is essentially invariant, with Class 1 remaining at unity across return periods, while higher classes exhibit progressively lower survival and increasing sensitivity to RP, preserving the expected ordinal hierarchy. The clearest separation occurs in Areia, where the upper tail shows a pronounced decay (Class 5: 0.242 at $\mathrm{RP}5$ to 0.128 at $\mathrm{RP}100$; Class 4: 0.924 to 0.532), yielding wide and decision-relevant spacing between classes. Paranhana maintains strict ordering with moderate and coherent return-period dependence, confirming that the five-class scale remains interpretable under independent hydro-geomorphic conditions. Jacuí retains monotonic decay within classes but displays a comparatively flat upper tier, echoing the Gravataí limitation and suggesting that Classes 4–5 may be pragmatically merged for preparedness mapping in this setting.

Beyond its methodological contributions, the fact that all input datasets are retrieved via open API and the workflow is fully automated, a screening-grade hazard map can be produced for any location covered by the Copernicus GLO-30 DEM and OpenStreetMap. This makes the framework particularly relevant to three practical contexts. First, in regional land-use planning, the five-class ordinal map can inform zoning restrictions and infrastructure assessments in data-scarce municipalities where no flood study exists, providing an evidence base where none was previously available. Second, in disaster-risk management and civil-defence operations, the upper hazard classes can serve as a first-pass delineation of priority evacuation and resource pre-positioning zones. Third, in infrastructure screening, transport and utility networks can be overlaid on the hazard layer to identify segments most exposed to inundation, enabling escape-route planning and maintenance interventions. Importantly, the result of the framework can be coupled with exposure and vulnerability datasets within IPCC risk workflows.

4 Conclusions

This study developed and evaluated a light-data framework that assembles globally available datasets, retrieved via API, into an automated, open-source flood-hazard workflow and returns standardised indices for direct coupling within IPCC-consistent risk assessments. The main conclusions are as follows:

1. The framework shows that globally available DEM- and OSM-based data can support a transferable flood-hazard workflow with limited data requirements. API-based retrieval makes the procedure reproducible, faster to deploy, scalable, and less prone to manual error.
2. Methodologically, the framework contributes an OSM-constrained drainage calibration for HAND, an explicit multi-resolution standardisation of MRVBF, and prototype score signatures that enable transferable, prototype-aware discretisation while preserving a common five-class ordinal scale.
3. The resulting zoning preserves useful discrimination skill beyond the calibration domains and maintains coherent behavioural ordering under independent validation, supporting its use as a planning-grade susceptibility layer. Its strength in the low-false-alarm regime particularly supports prioritisation of the upper classes for preparedness and targeted interventions.
4. From a practical standpoint, the framework is immediately deployable in data-scarce settings, requiring no local hydrological calibration, using only automated API-retrieved inputs. The standardised five-class output provides a first planning-grade hazard layer for zoning, civil-defence planning, and infrastructure screening where no prior assessment exists.

These conclusions should be read within the framework's intended scope. The product is a qualitative, screening-level propensity surface and does not replace design-grade hydrodynamic simulations. The next steps are to strengthen the standardisation strategy for domain selection and DEM conditioning and to extend the pipeline to future climate scenarios.

Code and data availability. The full source code, developed in Python v.3.11, is openly available under the Apache License 2.0 on GitHub at https://github.com/igorsiecz/PRIORF and has been archived in Zenodo at https://doi.org/10.5281/zenodo.18990241 (Moreira, 2025). The workflow retrieves the globally available input datasets required for the analysis. Elevation data are obtained from the Copernicus DEM GLO-30 collection through Google Earth Engine. Hydrographic features are retrieved from OpenStreetMap using OSMnx. The RP flood-extent maps used for model supervision and validation were provided by the Fundação Estadual de Planejamento Metropolitano e Regional

https://doi.org/10.5194/egusphere-2026-3884
Preprint. Discussion started: 3 August 2026

– METROPLAN. These maps are public governmental data from the Diretoria de Incentivo ao Desenvolvimento – DIRID/METROPLAN and may be requested by contacting diretoria-desenvolvimento@metroplan.rs.gov.br.

Appendix A: Predictor set used by the HGBR model

Table A1 summarises the predictors and monotonic constraints used to train the histogram-based gradient-boosting regressor.

Table A1. Predictor set used to train the histogram-based gradient-boosting regressor (HGBR). A positive sign indicates that the predicted susceptibility score is constrained to increase with increasing predictor value; a negative sign indicates the opposite; 0 indicates that no monotonic constraint was imposed

Predictor	Symbol or definition	Physical meaning	Monotonic constraint
HAND	HAND	Height above nearest drainage (m).	$-$
MRVBF	MRVBF	Multi-resolution valley-bottom flatness index.	0
Channel indicator	C_{ch}	Binary indicator derived from the hydrographic mask; equal to 1 for channel cells.	$+$
Channel distance	D_{ch}	Euclidean distance to the nearest channel cell (m).	$-$
Log-transformed channel distance	$\log D_{\mathrm{ch}} = \log(1 + D_{\mathrm{ch}})$	Log-transformed distance to the nearest channel cell.	$-$
Buffer indicator	B_{ch}	Binary riparian-corridor indicator; equal to 1 where $D_{\mathrm{ch}} \leq 100\,\mathrm{m}$.	$+$
Local floodplain fraction	F_{pl}	Local fraction of strongly planar cells, defined as $\mathrm{MRVBF} \geq 6$, within a $\sim 100\,\mathrm{m}$ moving window.	$+$
Reach-scale planarity	P_{ctx}	Mean fraction of strongly planar cells within the buffered corridor.	0
Reach-scale MRVBF percentile	$M_{\mathrm{ctx},90}$	90th percentile of MRVBF within the buffered corridor.	0
Planarity-adjusted HAND	$H_{\mathrm{adj},1} = \mathrm{HAND}/(1 + 0.75F_{\mathrm{pl}})$	HAND adjusted by local floodplain fraction to reduce effective vertical separation in planar settings.	0
Planarity-adjusted HAND	$H_{\mathrm{adj},2} = \mathrm{HAND}(1 - 0.5F_{\mathrm{pl}})$	Alternative HAND adjustment based on local floodplain fraction.	0
HAND–MRVBF interaction	$\mathrm{HAND} \times \mathrm{MRVBF}$	Interaction between vertical position relative to drainage and valley-bottom flatness.	0
Effective HAND	$H_{\mathrm{eff}} = \mathrm{HAND}/(10^{-3} + F_{\mathrm{pl}})$	Effective vertical separation that accentuates contrasts where the local floodplain fraction approaches zero.	0
Standardised HAND	H_z	Reach-wise standardised HAND, expressed as a z-score.	0
HAND percentile rank	H_{rank}	Empirical percentile rank of HAND within the analysis raster.	0

https://doi.org/10.5194/egusphere-2026-3884
Preprint. Discussion started: 3 August 2026

Author contributions. ISM: Conceptualization, Methodology, Software, Validation, Formal analysis, Investigation, Data curation, Writing – original draft. JC: Conceptualization, Methodology, Writing – review and editing. MET: Conceptualization, Methodology, Writing – review and editing. FD: Conceptualization, Methodology, Supervision. LATB: Conceptualization, Methodology, Writing – review and editing, Supervision.

Competing interests. The authors declare that they have no conflict of interest.

Acknowledgements. This work was carried out with the support of the National Council for Scientific and Technological Development – Brazil (CNPq), Process No. 131454/2023-4. The authors used OpenAI's ChatGPT to assist with the development of selected Python code and to improve the clarity and readability of the manuscript. During the preparation of this work, the authors used OpenAI's ChatGPT, including GPT-4 in early 2024 and GPT-5.5 Thinking in 2026, to assist with the development of selected Python code. The tool was also used for assistive language editing to improve sentence structure, clarity, and readability. All AI-assisted outputs were reviewed, edited, and, where applicable, tested by the authors, who take full responsibility for the manuscript and the underlying code. The authors also gratefully acknowledge Henrique Falck Grimm, MSc, for his valuable contributions to the early development of the methodological framework and for his insightful discussions during the preliminary conceptualisation of the study.

References

Ahmad, I., Farooq, R., Ashraf, M., Waseem, M., and Shangguan, D.: Improving Flood Hazard Susceptibility Assessment by Integrating Hydrodynamic Modeling with Remote Sensing and Ensemble Machine Learning, Natural Hazards, 121, 7839–7868, https://doi.org/10.1007/s11069-025-07109-2, 2025.

Albano, R., Limongi, C., Dal Sasso, S. F., Mancusi, L., and Adamowski, J.: Flood Scenario Spatio-Temporal Mapping via Hydrological and Hydrodynamic Modelling and a Remote Sensing Dataset: A Case Study of the Basento River (Southern Italy), International Journal of Disaster Risk Reduction, 111, 104 758, https://doi.org/10.1016/j.ijdrr.2024.104758, 2024.

Andreadis, K. M., Schumann, G. J.-P., Stampoulis, D., Bates, P. D., Brakenridge, G. R., and Kettner, A. J.: Can Atmospheric Reanalysis Data Sets Be Used to Reproduce Flooding Over Large Scales?, Geophysical Research Letters, 44, 10,369–10,377, https://doi.org/10.1002/2017GL075502, 2017.

Aristizabal, F., Salas, F., Petrochenkov, G., Grout, T., Avant, B., Bates, B., Spies, R., Chadwick, N., Wills, Z., and Judge, J.: Extending Height Above Nearest Drainage to Model Multiple Fluvial Sources in Flood Inundation Mapping Applications for the U.S. National Water Model, Water Resources Research, 59, e2022WR032 039, https://doi.org/10.1029/2022WR032039, 2023.

Azhar, M., Kane, B., Vahedifard, F., and AghaKouchak, A.: Comprehensive Portfolio of Adaptation Measures to Safeguard against Evolving Flood Risks in a Changing Climate, Communications Earth & Environment, 6, 824, https://doi.org/10.1038/s43247-025-02779-z, 2025.

Badillo-Rivera, E., Santiago, R., Poma, I., Chavez, T., Arroyo-Paz, A., Aucahuasi-Almidon, A., Hinostroza, E., Segura, E., Eyzaguirre, L., León, H., and Virú-Vásquez, P.: Flood Susceptibility Mapping in El Niño Phenomenom Integrating Multitemporal Radar Analysis, GIS and Machine Learning Techniques, Piura River Basin, Peru, Frontiers in Environmental Science, 13, https://doi.org/10.3389/fenvs.2025.1672107, 2025.

Bohorquez, P. and Del Moral-Erencia, J. D.: 100 Years of Competition between Reduction in Channel Capacity and Streamflow during Floods in the Guadalquivir River (Southern Spain), Remote Sensing, 9, 727, https://doi.org/10.3390/rs9070727, 2017.

Brivio, P. A., Colombo, R., Maggi, M., and Tomasoni, R.: Integration of Remote Sensing Data and GIS for Accurate Mapping of Flooded Areas, International Journal of Remote Sensing, 23, 429–441, https://doi.org/10.1080/01431160010014729, 2002.

Costache, R., Abdo, H. G., Pratap Mishra, A., Pal, S. C., Islam, A. R. M. T., Pande, C. B., Almohamad, H., Abdullah Al Dughairi, A., and Albanai, J. A.: Using Fuzzy and Machine Learning Iterative Optimized Models to Generate the Flood Susceptibility Maps: Case Study of Prahova River Basin, Romania, Geomatics, Natural Hazards and Risk, 14, 2281 241, https://doi.org/10.1080/19475705.2023.2281241, 2023.

Cunha, N. S., Magalhães, M. R., Domingos, T., Abreu, M. M., and Küpfer, C.: The Land Morphology Approach to Flood Risk Mapping: An Application to Portugal, Journal of Environmental Management, 193, 172–187, https://doi.org/10.1016/j.jenvman.2017.01.077, 2017.

Dávila-Hernández, S., González-Trinidad, J., Júnez-Ferreira, H. E., Bautista-Capetillo, C. F., de Ávila, H. M., Escareño, J. C., Ortiz-Letechipia, J., Rovelo, C. O. R., and López-Baltazar, E. A.: Effects of the Digital Elevation Model and Hydrological Processing Algorithms on the Geomorphological Parameterization, Water, 14, https://doi.org/10.3390/w14152363, 2022.

de Bruijn, K. M., Jafino, B. A., Merz, B., Doorn, N., Priest, S. J., Dahm, R. J., Zevenbergen, C., Aerts, J. C. J. H., and Comes, T.: Flood Risk Management through a Resilience Lens, Communications Earth & Environment, 3, 285, https://doi.org/10.1038/s43247-022-00613-4, 2022.

Erdbrügger, J., van Meerveld, I., Bishop, K., and Seibert, J.: Effect of DEM-smoothing and -Aggregation on Topographically-Based Flow Directions and Catchment Boundaries, Journal of Hydrology, 602, 126 717, https://doi.org/10.1016/j.jhydrol.2021.126717, 2021.

https://doi.org/10.5194/egusphere-2026-3884
Preprint. Discussion started: 3 August 2026

Esfandiari, M., Abdi, G., Jabari, S., McGrath, H., and Coleman, D.: Flood Hazard Risk Mapping Using a Pseudo Supervised Random Forest, Remote Sensing, 12, 3206, https://doi.org/10.3390/rs12193206, 2020.

Fatdillah, E., Rehan, B. M., Rameshwaran, P., Bell, V. A., Zulkafli, Z., Yusuf, B., and Sayers, P.: Spatial Estimates of Flood Damage and Risk Are Influenced by the Underpinning DEM Resolution: A Case Study in Kuala Lumpur, Malaysia, Water, 14, 2208, https://doi.org/10.3390/w14142208, 2022.

Gallant, J. C. and Dowling, T. I.: A Multiresolution Index of Valley Bottom Flatness for Mapping Depositional Areas, Water Resources Research, 39, https://doi.org/10.1029/2002WR001426, 2003.

Gianinetto, M., Villa, P., and Lechi, G.: Postflood Damage Evaluation Using Landsat TM and ETM+ Data Integrated with DEM, IEEE Transactions on Geoscience and Remote Sensing, 44, 236–243, https://doi.org/10.1109/TGRS.2005.859952, 2006.

Graf, W. L.: A Probabilistic Approach to the Spatial Assessment of River Channel Instability, Water Resources Research, 20, 953–962, https://doi.org/10.1029/WR020i007p00953, 1984.

Guan, M., Carrivick, J. L., Wright, N. G., Sleigh, P. A., and Staines, K. E. H.: Quantifying the Combined Effects of Multiple Extreme Floods on River Channel Geometry and on Flood Hazards, Journal of Hydrology, 538, 256–268, https://doi.org/10.1016/j.jhydrol.2016.04.004, 2016.

Guerschman, J., Warren, G., Byrne, G., Lymburner, L., Mueller, N., and Van Dijk, A.: MODIS-based Standing Water Detection for Flood and Large Reservoir Mapping: Algorithm Development and Applications for the Australian Continent, https://doi.org/10.4225/08/58518BD176131, 2011.

Guillaume Courty, L., Cesar Soriano-Monzalvo, J., and Pedrozo-Acuña, A.: Evaluation of Open-access Global Digital Elevation Models (AW3D30, SRTM, and ASTER) for Flood Modelling Purposes, Journal of Flood Risk Management, 12, e12 550, https://doi.org/10.1111/jfr3.12550, 2019.

Hajji, S., Krimissa, S., Abdelrahman, K., Boudhar, A., Elaloui, A., Ismaili, M., El Bouzekraoui, M., Chikh Essbiti, M., Kahal, A. Y., Mondal, B. K., and Namous, M.: Enhancing Flood Prediction through Remote Sensing, Machine Learning, and Google Earth Engine, Frontiers in Water, 7, https://doi.org/10.3389/frwa.2025.1514047, 2025.

Huang, C., Nguyen, B. D., Zhang, S., Cao, S., and Wagner, W.: A Comparison of Terrain Indices toward Their Ability in Assisting Surface Water Mapping from Sentinel-1 Data, ISPRS International Journal of Geo-Information, 6, 140, https://doi.org/10.3390/ijgi6050140, 2017.

IPCC: Climate Change 2022 – Impacts, Adaptation and Vulnerability: Working Group II Contribution to the Sixth Assessment Report of the Intergovernmental Panel on Climate Change, Cambridge University Press, 1 edn., ISBN 978-1-009-32584-4, https://doi.org/10.1017/9781009325844, 2023.

Islam, M. M. and Sado, K.: Flood Hazard Assessment in Bangladesh Using NOAA AVHRR Data with Geographical Information System, Hydrological Processes, 14, 605–620, https://doi.org/10.1002/(SICI)1099-1085(20000228)14:3<605::AID-HYP957>3.0.CO;2-L, 2000.

Johnson, J. M., Munasinghe, D., Eyelade, D., and Cohen, S.: An Integrated Evaluation of the National Water Model (NWM)–Height Above Nearest Drainage (HAND) Flood Mapping Methodology, Natural Hazards and Earth System Sciences, 19, 2405–2420, https://doi.org/10.5194/nhess-19-2405-2019, 2019.

Kim, D.-E., Gourbesville, P., and Liong, S.-Y.: Overcoming Data Scarcity in Flood Hazard Assessment Using Remote Sensing and Artificial Neural Network, Smart Water, 4, 2, https://doi.org/10.1186/s40713-018-0014-5, 2019.

Li, Z., Duque, F. Q., Grout, T., Bates, B., and Demir, I.: Comparative Analysis of Performance and Mechanisms of Flood Inundation Map Generation Using Height Above Nearest Drainage, Environmental Modelling & Software, 159, 105 565, https://doi.org/10.1016/j.envsoft.2022.105565, 2023.

https://doi.org/10.5194/egusphere-2026-3884
Preprint. Discussion started: 3 August 2026

M. C. Rápalo, L., Gomes Jr, M. N., and Mendiondo, E. M.: Developing an Open-Source Flood Forecasting System Adapted to Data-Scarce Regions: A Digital Twin Coupled with Hydrologic-Hydrodynamic Simulations, Journal of Hydrology, 644, 131 929, https://doi.org/10.1016/j.jhydrol.2024.131929, 2024.

Malone, B. P., McBratney, A. B., and Minasny, B.: Description and Spatial Inference of Soil Drainage Using Matrix Soil Colours in the Lower Hunter Valley, New South Wales, Australia, PeerJ, 6, e4659, https://doi.org/10.7717/peerj.4659, 2018.

McDermott, T. K. J.: Global Exposure to Flood Risk and Poverty, Nature Communications, 13, 3529, https://doi.org/10.1038/s41467-022-30725-6, 2022.

Merwade, V., Cook, A., and Coonrod, J.: GIS Techniques for Creating River Terrain Models for Hydrodynamic Modeling and Flood Inundation Mapping, Environmental Modelling & Software, 23, 1300–1311, https://doi.org/10.1016/j.envsoft.2008.03.005, 2008.

Miranda, F., Franco, A. B., Rezende, O., da Costa, B. B. F., Najjar, M., Haddad, A. N., and Miguez, M.: A GIS-Based Index of Physical Susceptibility to Flooding as a Tool for Flood Risk Management, Land, 12, 1408, https://doi.org/10.3390/land12071408, 2023.

Moreira, I. S.: PRIORI - Protocol for Road Infrastructure Operational Risk Due to Inundation, Zenodo, https://doi.org/10.5281/ZENODO.17515623, 2025.

Navarro, J. S., Zhuang, R., Albertini, C., and Manfreda, S.: Mapping Flood Susceptibility Using Random Forest Exploiting Satellite Observations and Geomorphic Features, Science of The Total Environment, 1002, 180 592, https://doi.org/10.1016/j.scitotenv.2025.180592, 2025.

Nobre, A. D., Cuartas, L. A., Hodnett, M., Rennó, C. D., Rodrigues, G., Silveira, A., Waterloo, M., and Saleska, S.: Height Above the Nearest Drainage – a Hydrologically Relevant New Terrain Model, Journal of Hydrology, 404, 13–29, https://doi.org/10.1016/j.jhydrol.2011.03.051, 2011.

Peña, F., Nardi, F., Melesse, A., and Obeysekera, J.: Assessing Geomorphic Floodplain Models for Large Scale Coarse Resolution 2D Flood Modelling in Data Scarce Regions, Geomorphology, 389, 107 841, https://doi.org/10.1016/j.geomorph.2021.107841, 2021.

Rahmani, S. R., Ackerson, J. P., Schulze, D., Adhikari, K., and Libohova, Z.: Digital Mapping of Soil Organic Matter and Cation Exchange Capacity in a Low Relief Landscape Using LiDAR Data, Agronomy, 12, https://doi.org/10.3390/agronomy12061338, 2022.

Razavi-Termeh, S. V., Sadeghi-Niaraki, A., Abba, S. I., Hussain, J., and Choi, S.-M.: Flood-Prone Area Mapping Using a Synergistic Approach with Swarm Intelligence and Gradient Boosting Algorithms, Scientific Reports, 15, 27 924, https://doi.org/10.1038/s41598-025-12022-6, 2025.

Rennó, C. D., Nobre, A. D., Cuartas, L. A., Soares, J. V., Hodnett, M. G., Tomasella, J., and Waterloo, M. J.: HAND, a New Terrain Descriptor Using SRTM-DEM: Mapping Terra-Firme Rainforest Environments in Amazonia, Remote Sensing of Environment, 112, 3469–3481, https://doi.org/10.1016/j.rse.2008.03.018, 2008.

Sabeh, H., Abdallah, C., Chahinian, N., Tournoud, M.-G., Hdeib, R., and Moussa, R.: Evaluating Terrain-Based HAND-SRC Flood Mapping Model in Low-Relief Rural Plains Using High Resolution Topography and Crowdsourced Data, Journal of Hydrology, 652, 132 649, https://doi.org/10.1016/j.jhydrol.2024.132649, 2025.

Saravanan, S. and Abijith, D.: Flood Susceptibility Mapping of Northeast Coastal Districts of Tamil Nadu India Using Multi-source Geospatial Data and Machine Learning Techniques, Geocarto International, 37, 15 252–15 281, https://doi.org/10.1080/10106049.2022.2096702, 2022.

Stocker, T.: Climate Change 2013: The Physical Science Basis: Working Group I Contribution to the Fifth Assessment Report of the Intergovernmental Panel on Climate Change, Cambridge University Press, ISBN 978-1-107-05799-9, 2014.

https://doi.org/10.5194/egusphere-2026-3884
Preprint. Discussion started: 3 August 2026

Tang, X., Li, J., Liu, M., Liu, W., and Hong, H.: Flood Susceptibility Assessment Based on a Novel Random Naïve Bayes Method: A Comparison between Different Factor Discretization Methods, CATENA, 190, 104 536, https://doi.org/10.1016/j.catena.2020.104536, 2020.

Tufano, R., Guerriero, L., Annibali Corona, M., Cianflone, G., Di Martire, D., Ietto, F., Novellino, A., Rispoli, C., Zito, C., and Calcaterra, D.: Multiscenario Flood Hazard Assessment Using Probabilistic Runoff Hydrograph Estimation and 2D Hydrodynamic Modelling, Natural Hazards, 116, 1029–1051, https://doi.org/10.1007/s11069-022-05710-3, 2023.

van Ginkel, K. C. H., Dottori, F., Alfieri, L., Feyen, L., and Koks, E. E.: Flood Risk Assessment of the European Road Network, Natural Hazards and Earth System Sciences, 21, 1011–1027, https://doi.org/10.5194/nhess-21-1011-2021, 2021.

Vázquez-Tarrío, D., Ruiz-Villanueva, V., Garrote, J., Benito, G., Calle, M., Lucía, A., and Díez-Herrero, A.: Effects of Sediment Transport on Flood Hazards: Lessons Learned and Remaining Challenges, Geomorphology, 446, 108 976, https://doi.org/10.1016/j.geomorph.2023.108976, 2024.

Wang, Y., Colby, J. D., and Mulcahy, K. A.: An Efficient Method for Mapping Flood Extent in a Coastal Floodplain Using Landsat TM and DEM Data, International Journal of Remote Sensing, 23, 3681–3696, https://doi.org/10.1080/01431160110114484, 2002.

Wang, Y., Li, Z., Tang, Z., and Zeng, G.: A GIS-Based Spatial Multi-Criteria Approach for Flood Risk Assessment in the Dongting Lake Region, Hunan, Central China, Water Resources Management, 25, 3465–3484, https://doi.org/10.1007/s11269-011-9866-2, 2011.

Werner, M. G. F.: Impact of Grid Size in GIS Based Flood Extent Mapping Using a 1D Flow Model, Physics and Chemistry of the Earth, Part B: Hydrology, Oceans and Atmosphere, 26, 517–522, https://doi.org/10.1016/S1464-1909(01)00043-0, 2001.

Zhang, H. and Huang, G.: Building channel networks for flat regions in digital elevation models, Hydrological Processes, 23, 2879–2887, https://doi.org/10.1002/hyp.7378, 2009.

Zhang, X., Wan, H., Zwiers, F. W., Hegerl, G. C., and Min, S.-K.: Attributing Intensification of Precipitation Extremes to Human Influence, Geophysical Research Letters, 40, 5252–5257, https://doi.org/10.1002/grl.51010, 2013.

Zhao, T., Shao, Q., and Zhang, Y.: Deriving Flood-Mediated Connectivity between River Channels and Floodplains: Data-Driven Approaches, Scientific Reports, 7, 43 239, https://doi.org/10.1038/srep43239, 2017.